arXiv:1405.2139v1 [physics.flu-dyn] 9 May 2014

Relative-Periodic Elastic Collisions of Water Waves

Jon Wilkening

ABSTRACT. We compute time-periodic and relative-periodic solutions of the free-surface Euler equations that take the form of overtaking collisions of unidirectional solitary waves of different amplitude on a periodic domain. As a starting guess, we superpose two Stokes waves offset by half the spatial period. Using an overdetermined shooting method, the background radiation generated by collisions of the Stokes waves is tuned to be identical before and after each collision. In some cases, the radiation is effectively eliminated in this procedure, yielding smooth soliton-like solutions that interact elastically forever. We find examples in which the larger wave subsumes the smaller wave each time they collide, and others in which the trailing wave bumps into the leading wave, transferring energy without fully merging. Similarities notwithstanding, these solutions are found quantitatively to lie outside of the Korteweg-de Vries regime. We conclude that quasi-periodic elastic collisions are not unique to integrable model water wave equations when the domain is periodic.

1. Introduction

A striking feature of multiple-soliton solutions of integrable model equations such as the Korteweg-deVries equation, the Benjamin-Ono equation, and the nonlinear Schrödinger equation is that they interact elastically, leading to time-periodic, relative-periodic, or quasi-periodic dynamics. By contrast, the interaction of solitary waves for the free-surface Euler equations is inelastic. However, it has been observed many times in the literature [**10, 13, 35, 44, 38, 53, 15, 37**] that the residual radiation after a collision of such solitary waves can be remarkably small. In the present paper we explore the possibility of finding nearby time-periodic and relative-periodic solutions of the Euler equations using a collision of unidirectional Stokes waves as a starting guess. Such solutions demonstrate that recurrent elastic collisions of solitary waves in the spatially periodic case do not necessarily indicate that the underlying system is integrable.

A relative-periodic solution is one that returns to a spatial phase shift of its initial condition at a later time. This only makes sense on a periodic domain, where the waves collide repeatedly at regular intervals in both time and space, with the locations of the collisions drifting steadily in time. They are special cases (with $N = 2$) of quasi-periodic solutions, which have the form $u(x,t) = U(\vec{\kappa}x + \vec{\omega}t + \vec{\alpha})$

with U an N-periodic continuous function, i.e. $U \in C(\mathbb{T}^N)$, and $\vec{\kappa}, \vec{\omega}, \vec{\alpha} \in \mathbb{R}^N$. Throughout the manuscript, we will use the phrase "solitary waves" in a broad sense to describe waves that, most of the time, remain well-separated from one another and propagate with nearly constant speed and shape. "Stokes waves" will refer to periodic progressive solutions of the free-surface Euler equations of permanent form, or waves that began at $t = 0$ as a linear superposition of such traveling waves. They comprise a special class of solitary waves. "Solitons" will refer specifically to superpositions of sech^2 solutions of the KdV equation on the whole line, while "cnoidal solutions" will refer to their spatially periodic, multi-phase counterparts; see §5 for elaboration.

It was found in [**49**] that decreasing the fluid depth causes standing waves to transition from large-scale symmetric sloshing behavior in deep water to pairs of counter-propagating solitary waves that collide repeatedly in shallow water. In the present work, we consider unidirectional waves of different amplitude that collide due to taller waves moving faster than shorter ones. We present two examples of solutions of this type: one where the resulting dynamics is fully time-periodic; and one where it is relative-periodic, returning to a spatial phase shift of the initial condition at a later time. Both examples exhibit behavior typical of collisions of KdV solitons. In the first, one wave is significantly larger than the other, and completely subsumes it during the interaction. In the second, the waves have similar amplitude, with the trailing wave bumping into the leading wave and transferring energy without fully merging.

Despite these similarities, the amplitude of the waves in our examples are too large for the assumptions in the derivation of the KdV equation to hold. In particular, the larger wave in the first example is more than half the fluid depth in height, and there is significant vertical motion of the fluid when the waves pass by. A detailed comparison of the Euler and KdV equations for waves with these properties is carried out in §5. A review of the literature on water wave collisions and the accuracy of the KdV model of water waves is also given in that section.

Rather than compute such solutions by increasing the amplitude from the linearized regime via numerical continuation, as was done for counter-propagating waves in [**49**], we use collisions of right-moving Stokes waves as starting guesses. The goal is to minimally "tune" the background radiation generated by the Stokes collisions so that the amount coming out of each collision is identical to what went into it. In the first example of §4, we find that the tuned background radiation takes the form of a train of traveling waves of smaller wavelength moving to the right more slowly than either solitary wave. By contrast, in the counter-propagating case studied in [**49**], it consists of an array of smaller-wavelength standing waves oscillating rapidly relative to the time between collisions of the primary waves. In the second example of §4, the background radiation is essentially absent, which is to say that the optimized solution is free from high-frequency, low-amplitude disturbances in the trough, and closely resembles a relative-periodic cnoidal solution of KdV. We call the collisions in this solution "elastic" as they repeat forever, unchanged up to spatial translation, and there are no features to distinguish radiation from the waves themselves. This process of tuning parameters to minimize or eliminate small-amplitude oscillations in the wave troughs is reminiscent of Vanden-Broeck's work [**45**] in which oscillations at infinity could be eliminated from solitary capillary-gravity waves by choosing the amplitude appropriately.

To search for relative periodic solutions, we use a variant of the overdetermined shooting method developed by the author and collaborators in previous work to study several related problems: time-periodic solutions of the Benjamin-Ono equation [**5**, **3**] and the vortex sheet with surface tension [**4**, **6**]; Hopf bifurcation and stability transitions in mode-locked lasers [**50**]; cyclic steady-states in rolling treaded tires [**21**]; self-similarity (or lack thereof) at the crests of large-amplitude standing water waves [**47**]; harmonic resonance and spontaneous nucleation of new branches of standing water waves at critical depths [**49**]; and three-dimensional standing water waves [**42**]. The three approaches developed in these papers are the adjoint continuation method [**5**, **50**], a Newton-Krylov shooting method [**21**], and a trust region shooting method [**49**] based on the Levenberg-Marquardt algorithm [**39**]. We adopt the latter method here to exploit an opportunity to consolidate the work in computing the Dirichlet-Neumann operator for many columns of the Jacobian simultaneously, in parallel.

One computational novelty of this work is that we search directly for large-amplitude solutions of a nonlinear two-point boundary value problem, without using numerical continuation to get there. This is generally difficult. However, in the present case, numerical continuation is also difficult due to non-smooth bifurcation "curves" riddled with Cantor-like gaps [**41**], and the long simulation times that occur between collisions in the unidirectional case. Our shooting method has proven robust enough to succeed in finding time-periodic solutions, when they exist, with a poor starting guess. False positives are avoided by resolving the solutions spectrally to machine accuracy and overconstraining the minimization problem. Much of the challenge is in determining the form of the initial condition and the objective function to avoid wandering off in the wrong direction and falling into a nonzero local minimum before locking onto a nearby relative-periodic solution.

2. Equations of motion

The equations of motion of a free surface $\eta(x, t)$ evolving over an ideal fluid with velocity potential $\phi(x, y, t)$ may be written [**46**, **27**, **17**, **18**]

$$(2.1) \qquad \eta_t = \phi_y - \eta_x \phi_x,$$
$$\varphi_t = P \left[\phi_y \eta_t - \frac{1}{2} \phi_x^2 - \frac{1}{2} \phi_y^2 - g\eta \right],$$

where subscripts denote partial derivatives, $\varphi(x, t) = \phi(x, \eta(x, t), t)$ is the restriction of ϕ to the free surface, $g = 1$ is the acceleration of gravity, $\rho = 1$ is the fluid density, and P is the projection

$$(2.2) \qquad Pf = f - \frac{1}{2\pi} \int_0^{2\pi} f(x) \, dx,$$

where we assume a 2π-periodic domain. The velocity components $u = \phi_x$ and $v = \phi_y$ at the free surface can be computed from φ via

$$(2.3) \qquad \begin{pmatrix} \phi_x \\ \phi_y \end{pmatrix} = \frac{1}{1 + \eta'(x)^2} \begin{pmatrix} 1 & -\eta'(x) \\ \eta'(x) & 1 \end{pmatrix} \begin{pmatrix} \varphi'(x) \\ \mathcal{G}\varphi(x) \end{pmatrix},$$

where a prime denotes a derivative and $\mathcal{G}$ is the Dirichlet-Neumann operator [**16**]

$$(2.4) \qquad \mathcal{G}\varphi(x) = \sqrt{1 + \eta'(x)^2} \, \frac{\partial \phi}{\partial n}(x + i\eta(x)) = \phi_y - \eta_x \phi_x$$

for the Laplace equation, with periodic boundary conditions in x, Dirichlet conditions ($\phi = \varphi$) on the upper boundary, and Neumann conditions ($\phi_y = 0$) on the lower boundary, assumed flat. We have suppressed t in the notation since time is frozen in the Laplace equation. We compute $\mathcal{G}\varphi$ using a boundary integral collocation method [**34, 7, 30, 36, 8**] and advance the solution in time using an 8th order Runge-Kutta scheme [**23**] with 36th order filtering [**25**]. See [**49**] for details.

3. Computation of relative-periodic solutions

Traveling waves have the symmetry that

$$(3.1) \qquad \eta(x,0) \text{ is even}, \qquad \varphi(x,0) \text{ is odd}.$$

This remains true if x is replaced by $x - \pi$. As a starting guess for a new class of time-periodic and relative-periodic solutions, we have in mind superposing two traveling waves, one centered at $x = 0$ and the other at $x = \pi$. Doing so will preserve the property (3.1), but the waves will now interact rather than remain pure traveling waves. A solution will be called *relative periodic* if there exists a time T and phase shift θ such that

$$(3.2) \qquad \eta(x, t+T) = \eta(x - \theta, t), \qquad \varphi(x, t+T) = \varphi(x - \theta, t)$$

for all t and x. Time-periodicity is obtained as a special case, with $\theta \in 2\pi\mathbb{Z}$. We can save a factor of 2 in computational work by imposing the alternative condition

$$(3.3) \qquad \eta(x + \theta/2, T/2) \text{ is even}, \qquad \varphi(x + \theta/2, T/2) \text{ is odd}.$$

From this, it follows that

$$\eta(x + \theta/2, T/2) = \eta(-x + \theta/2, T/2) = \eta(x - \theta/2, -T/2),$$
$$\varphi(x + \theta/2, T/2) = -\varphi(-x + \theta/2, T/2) = \varphi(x - \theta/2, -T/2).$$

But then both sides of each equation in (3.2) agree at time $t = -T/2$. Thus, (3.2) holds for all time.

In the context of traveling-standing waves in deep water [**48**], it is natural to define T as twice the value above, replacing all factors of $T/2$ by $T/4$. That way a pure standing wave returns to its original configuration in time T instead of shifting in space by π in time T. In the present work, we consider pairs of solitary waves moving to the right at different speeds, so it is more natural to define T as the first (rather than the second) time there exists a θ such that (3.2) holds.

3.1. Objective function. We adapt the overdetermined shooting method of [**47, 49**] to compute solutions of (3.1)–(3.3). This method employs the Levenberg-Marquardt method [**39**] with delayed Jacobian updates [**49**] to solve the nonlinear least squares problem described below.

For (3.1), we build the symmetry into the initial conditions over which the shooting method is allowed to search: we choose an integer n and consider initial conditions of the form

$$(3.4) \qquad \hat{\eta}_k(0) = c_{2|k|-1}, \qquad \hat{\varphi}_k(0) = \pm i c_{2|k|},$$

where $k \in \{\pm 1, \pm 2, \ldots, \pm \frac{n}{2}\}$ and $\hat{\eta}_k(t)$, $\hat{\varphi}_k(t)$ are the Fourier modes of $\eta(x,t)$, $\varphi(x,t)$. The numbers $c_1, \ldots, c_n$ are assumed real and all other Fourier modes (except $\hat{\eta}_0$) are zero. We set $\hat{\eta}_0$ to the fluid depth so that $y = 0$ is a symmetry line

corresponding to the bottom wall. This is convenient for computing the Dirichlet-Neumann operator [**49**]. In the formula for $\hat{\varphi}_k$, the minus sign is taken if $k < 0$ so that $\hat{\varphi}_{-k} = \overline{\hat{\varphi}_k}$. We also solve for the period,

$$(3.5) \qquad\qquad T = c_{n+1}.$$

The phase shift θ is taken as a prescribed parameter here. Alternatively, in a study of traveling-standing waves [**48**], the author defines a traveling parameter β and varies $\theta = c_{n+2}$ as part of the algorithm to obtain the desired value of β. This parameter β is less meaningful for solitary wave collisions in shallow water, so we use θ itself as the traveling parameter in the present study. We also need to specify the amplitude of the wave. This can be done in various ways, e.g. by specifying the value of the energy,

$$E = \frac{1}{2\pi} \int_0^{2\pi} \tfrac{1}{2}\varphi\mathcal{G}\varphi + \tfrac{1}{2}g\eta^2 \, dx,$$

by constraining a Fourier mode such as $\hat{\eta}_1(0)$, or by specifying the initial height of the wave at $x = 0$:

$$\eta(0,0) = \hat{\eta}_0 + \sum_{k=1}^{n/2} 2c_{2k-1}.$$

Thus, to enforce (3.3), we can minimize the objective function

$$(3.6) \qquad\qquad f(c) = \frac{1}{2} r(c)^T r(c),$$

where

$$(3.7) \qquad r_1 = \big(\ \text{choose one:} \quad E - a \quad, \quad \hat{\eta}_1(0) - a \quad, \quad \eta(0,0) - a\ \big),$$

$$r_{2j} = \text{Im}\{e^{ij\theta/2}\hat{\eta}_j(T/2)\}, \qquad r_{2j+1} = \text{Re}\{e^{ij\theta/2}\hat{\varphi}_j(T/2)\}, \qquad (1 \le j \le M/2).$$

Here a is the desired value of the chosen amplitude parameter. Alternatively, we can impose (3.2) directly by minimizing

$$(3.8) \ \ \tilde{f} = \frac{1}{2}r_1^2 + \frac{1}{4\pi} \int_0^{2\pi} \left(\big[\eta(x,T) - \eta(x - \theta,0)\big]^2 + \big[\varphi(x,T) - \varphi(x - \theta,0)\big]^2 \right) dx,$$

which also takes the form $\frac{1}{2}r^T r$ if we define r_1 as above and

$$(3.9) \qquad \begin{aligned} r_{4j-2} + ir_{4j-1} &= \sqrt{2}\left[\hat{\eta}_j(T) - e^{-ij\theta}\hat{\eta}_j(0)\right], \\ r_{4j} + ir_{4j+1} &= \sqrt{2}\left[\hat{\varphi}_j(T) - e^{-ij\theta}\hat{\varphi}_j(0)\right], \end{aligned} \qquad (1 \le j \le M/2).$$

Note that f measures deviation from evenness and oddness of $\eta(x + \theta/2, T/2)$ and $\varphi(x + \theta/2, T/2)$, respectively, while $\tilde{f}$ measures deviation of $\eta(x + \theta, T)$ and $\varphi(x + \theta, T)$ from their initial states. In the first example of §4, we minimize $\tilde{f}$ directly, while in the second we minimize f and check that $\tilde{f}$ is also small, as a means of validation. The number of equations, $m = M + 1$ for f and $m = 2M + 1$ for $\tilde{f}$, is generally larger than the number of unknowns, $n + 1$, due to zero-padding of the initial conditions. This adds robustness to the shooting method and causes all Fourier modes varied by the algorithm, namely those in (3.4), to be well-resolved on the mesh.

3.2. Computation of the Jacobian. To compute the kth column of the Jacobian $J = \nabla_c r$, which is needed by the Levenberg-Marquardt method, we solve the linearized equations along with the nonlinear ones:

$$(3.10) \qquad \frac{\partial}{\partial t}\begin{pmatrix} q \\ \dot{q} \end{pmatrix} = \begin{pmatrix} F(q) \\ DF(q)\dot{q} \end{pmatrix}, \qquad \begin{matrix} q(0) = q_0 = (\eta_0, \varphi_0), \\ \dot{q}(0) = \dot{q}_0 = \partial q_0/\partial c_k. \end{matrix}$$

Here $q = (\eta, \varphi)$, $\dot{q} = (\dot{\eta}, \dot{\varphi})$, $F(q)$ is given in (2.1), DF is its derivative (see [**49**] for explicit formulas), and a dot represents a variational derivative with respect to perturbation of the initial conditions, not a time derivative. To compute $\partial r_i/\partial c_k$ for $i \geq 2$ and $k \leq n$, one simply puts a dot over each Fourier mode on the right-hand side of (3.7) or (3.9), including $\hat{\eta}_j(0)$ and $\hat{\varphi}_j(0)$ in (3.9). If $k = n+1$, then $c_k = T$ and

$$\frac{\partial r_{2j}}{\partial T} = \mathrm{Im}\{e^{ij\theta/2}(1/2)\partial_t\hat{\eta}_j(T/2)\}, \qquad \frac{\partial(r_{4j} + ir_{4j+1})}{\partial T} = \sqrt{2}\left[\partial_t\hat{\varphi}_j(T)\right]$$

in (3.7) and (3.9), respectively, with similar formulas for $\partial(r_{4j-2} + ir_{4j-1})/\partial T$ and $\partial r_{2j+1}/\partial T$. The three possibilities for r_1 are handled as follows:

$$\text{case 1:} \quad \frac{\partial r_1}{\partial c_k} = \dot{E} = \frac{1}{2\pi}\int_0^{2\pi} [\dot{\varphi}\eta_t - \dot{\eta}\varphi_t]_{t=0}\, dx, \quad (k \leq n), \qquad \frac{\partial r_1}{\partial c_{n+1}} = 0,$$

$$\text{case 2:} \quad \frac{\partial r_1}{\partial c_k} = \dot{\hat{\eta}}_1(0) = \delta_{k,1}, \quad (k \leq n+1),$$

$$\text{case 3:} \quad \frac{\partial r_1}{\partial c_k} = \dot{\eta}(0,0) = 2\delta_{k,\mathrm{odd}}, \quad (k \leq n), \qquad \frac{\partial r_1}{\partial c_{n+1}} = 0,$$

where $\delta_{k,j}$ and $\delta_{k,\mathrm{odd}}$ equal 1 if $k = j$ or k is odd, respectively, and equal zero otherwise. The vectors $\dot{q}$ in (3.10) are computed in batches, each initialized with a different initial perturbation, to consolidate the work in computing the Dirichlet-Neumann operator during each timestep. See [**49, 48**] for details.

4. Numerical results

As mentioned in the introduction, our idea is to use collisions of unidirectional Stokes (i.e. traveling) waves as starting guesses to find time-periodic and relative periodic solutions of the Euler equations. We begin by computing traveling waves of varying wave height and record their periods. This is easily done in the framework of §3. We set $\theta = \pi/64$ (or any other small number) and minimize $\tilde{f}$ in (3.8). The resulting "period" T will give the wave speed via $c = \theta/T$. Below we report $T = 2\pi c$, i.e. T is rescaled as if θ were 2π. We control the amplitude by specifying $\hat{\eta}_1(0)$, which is the second option listed in §3 for defining the first component r_1 of the residual. A more conventional approach for computing traveling waves is to substitute $\eta(x - ct)$, $\varphi(x - ct)$ into (2.1) and solve the resulting stationary problem (or an equivalent integral equation) by Newton's method [**12, 11, 37**]. Note that the wave speed c here is unrelated to the vector c of unknowns in (3.4).

With traveling waves in hand, out next goal is to collide two of them and search for a nearby time-periodic solution, with $\theta = 0$. As shown in Figure 1, varying $\hat{\eta}_1(0)$ from 0 to 7.4×10^{-4} causes the period of a Stokes wave with wavelength $\lambda = 2\pi$ and mean fluid depth $h = 0.05$ to decrease from $T_O = 28.1110$ to $T_A = 22.9739$, and the wave height (vertical crest-to-trough distance) to increase from 0 to 0.02892. Solution C is the closest among the Stokes waves we computed to satisfying $5T_C = 6T_A$, where $p = 5$ is the smallest integer satisfying $\frac{p+1}{p}T_A < T_O$. We then combine
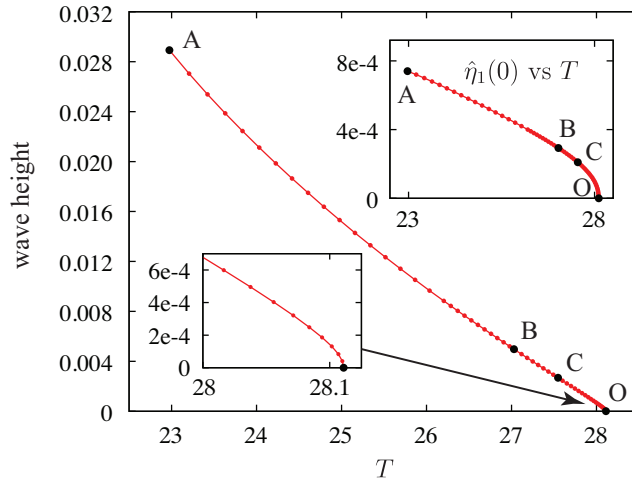
FIGURE 1. Plots of wave height and first Fourier mode versus period for Stokes waves with wavelength 2π and fluid depth $h = 0.05$. The temporal periods are $6T_A = 137.843 \approx 137.738 = 5T_C$.
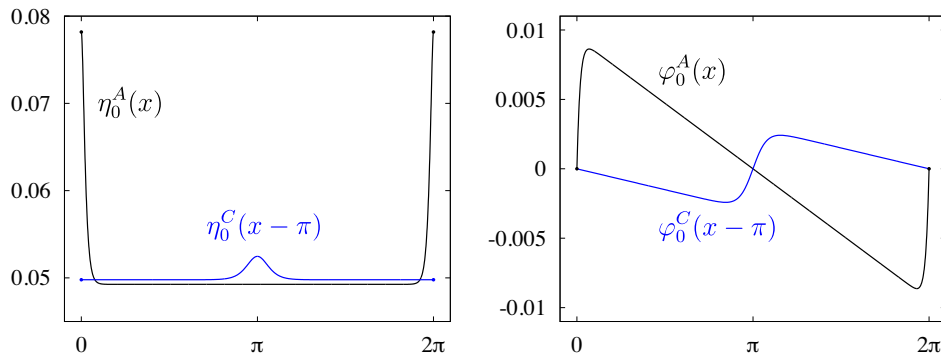

FIGURE 2. Wave profile and velocity potential of Stokes waves labeled A and C in Fig. 1, plotted over one spatial period at $t = 0$.

solution A with a spatial phase shift of solution C at $t = 0$. The resulting initial conditions are

$$(4.1) \quad \begin{aligned} \eta_0^{A+C}(x) &= h + \left[\eta_0^A(x) - h\right] + \left[\eta_0^C(x - \pi) - h\right], \\ \varphi_0^{A+C}(x) &= \varphi_0^A(x) + \varphi_0^C(x - \pi), \end{aligned}$$

where $h = 0.05$ is the mean fluid depth. Plots of $\eta_0^A(x)$, $\eta_0^C(x - \pi)$, $\varphi_0^A(x)$ and $\varphi_0^C(x-\pi)$ are shown in Figure 2. If the waves did not interact, the combined solution would be time-periodic (to the extent that $5T_C = 6T_A$, i.e. to about 0.076%). But the waves do interact. In addition to the complicated interaction that occurs when they collide, each slows the other down between collisions by introducing a negative gradient in the velocity potential between its own wave crests. Indeed, as shown in the right panel of Figure 2, the velocity potential increases rapidly across a right-moving solitary wave and decreases elsewhere to achieve spatial periodicity. The
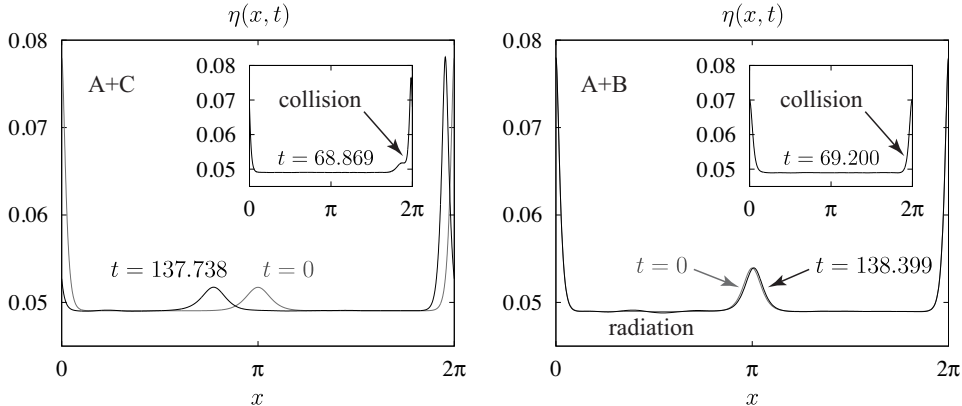
FIGURE 3.   Collision of two right-moving Stokes waves that nearly
return to their initial configuration after the interaction. (left) So-
lutions A and C were combined via (4.1) and evolved through one
collision to $t = 137.738$. (right) Through trial and error, we ad-
justed the amplitude of the smaller Stokes wave and the simulation
time to obtain a nearly time-periodic solution.

decreasing velocity potential induces a background flow opposite to the direction
of travel of the other wave. In the left panel of Figure 3, we see that the net effect
is that neither of the superposed waves has returned to its starting position at
$t = 5T_C$, and the smaller wave has experienced a greater net decrease in speed.
However, as shown in the right panel, by adjusting the amplitude of the smaller
wave (replacing solution C by B) and increasing T slightly to 138.399, we are able
to hand-tune the Stokes waves to achieve $\tilde{f} \approx 5.5 \times 10^{-8}$, where θ is set to zero in
(3.8). Note that as t varies from 0 to $T/10$ in the left panel of Figure 4, the small
wave advances by π units to the right while the large wave advances by 1.2π units.
The waves collide at $t = T/2$. This generates a small amount of radiation, which
can be seen at $t = T$ in the right panel of Figure 3. Some radiation behind the
large wave is present for all $t > 0$, as shown in Figure 5.

Before minimizing $\tilde{f}$, we advance the two Stokes waves to the time of the first
collision, $t = T/2$. At this time, the larger solitary wave has traversed the domain 3
times and the smaller one 2.5 times, so their peaks lie on top of each other at $x = 0$.
The reason to do this is that when the waves merge, the combined wave is shorter,
wider, and smoother than at any other time during the evolution. Quantitatively,
the Fourier modes of $\hat{\eta}_k(t)$ and $\hat{\varphi}_k(t)$ decay below 10^{-15} for $k \geq 600$ at $t = 0$,
and $k \geq 200$ when $t = T/2$. Thus, the number of columns needed in the Jacobian
is reduced by a factor of 3, and the problem becomes more overdetermined, hence
more robust. For the calculation of a time-periodic solution, we let $t = 0$ correspond
to this merged state, which affects the time labels when comparing Figures 4 and 6.
As a final initialization step, we project onto the space of initial conditions satisfying
(3.4) by zeroing out the imaginary parts of $\hat{\eta}_k(0)$ and the real parts of $\hat{\varphi}_k(0)$, which
are already small. Surprisingly, this improves the time-periodicity of the initial
guess in (3.8) to $\tilde{f} = 2.3 \times 10^{-8}$.

We emphasize that our goal is to find *any* nearby time-periodic solution by
adjusting the initial conditions to drive $\tilde{f}$ to zero. Energy will be conserved as the
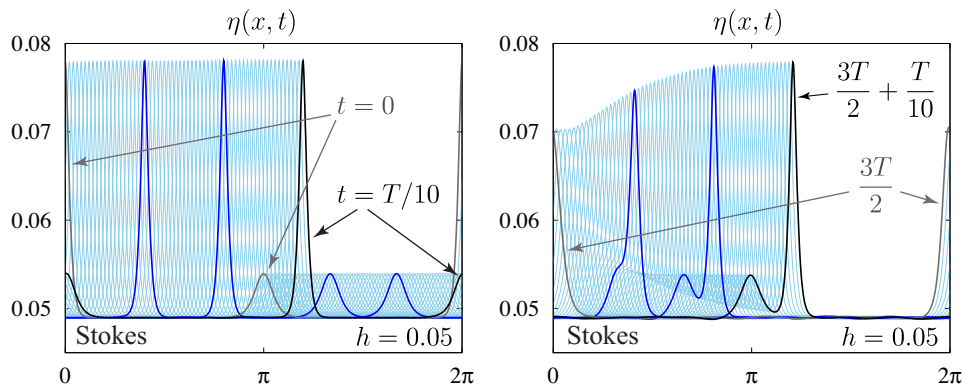
FIGURE 4. Evolution of two Stokes waves that collide repeatedly, at times $t \approx T/2 + kT$, $k \geq 0$. (left) Traveling solutions A and B in Figure 1 were initialized with wave crests at $x = 0$ and $x = \pi$, respectively. The combined solution is approximately time-periodic, with period $T = 138.399$. (right) The same solution, at later times, starting with the second collision $(t = 3T/2)$.
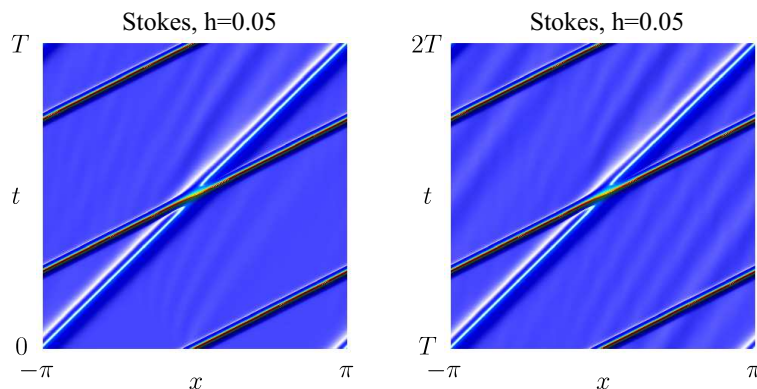

FIGURE 5. A different view of the solutions in Figure 4 shows the generation of background waves. Shown here are the functions $\eta(x + 8\pi t/T, t)$, which give the dynamics in a frame moving to the right fast enough to traverse the domain four times in time T. In a stationary frame, the smaller and larger solitary waves traverse the domain 5 and 6 times, respectively.

solution evolves from a given initial condition, but is only imposed as a constraint (in the form of a penalty) on the search for initial conditions when the first component of the residual in (3.7) is set to $r_1 = E - a$. In the present calculation, we use $r_1 = \eta(0, 0) - a$ instead. In the second example, presented below, we will constrain energy. In either case, projecting onto the space of initial conditions satisfying (3.4) can cause r_1 to increase, but it will decrease to zero in the course of minimizing $\tilde{f}$. This projection is essential for the symmetry arguments of §3.1 to work.
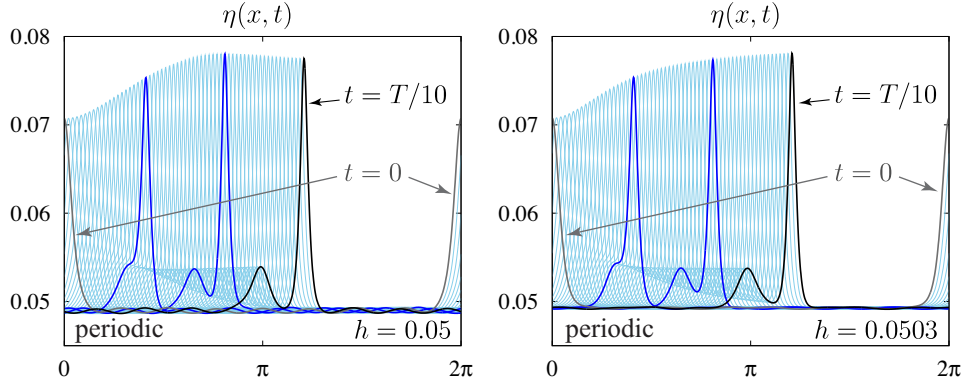
FIGURE 6.   Time-periodic solutions near the Stokes waves of Figure 4.   (left) $h = 0.05$, $\eta(0,0) = 0.0707148$, $T = 138.387$, $\tilde{f} = 4.26 \times 10^{-27}$.   (right) $h = 0.0503$, $\eta(0,0) = 0.0707637$, $T = 138.396$, $\tilde{f} = 1.27 \times 10^{-26}$. The background radiation was minimized by hand in the right panel by varying h and $\eta(0,0)$.
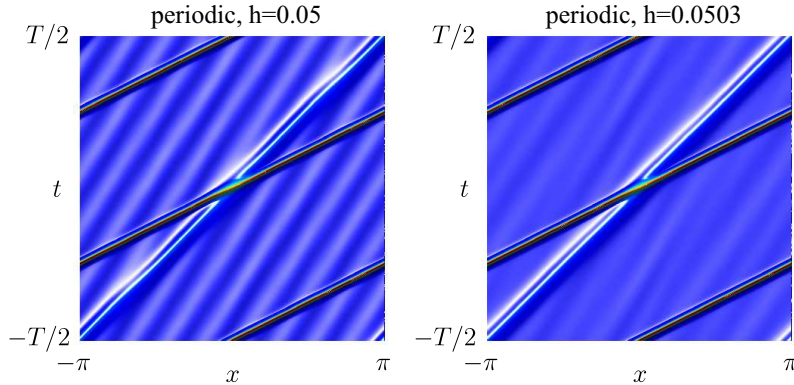

FIGURE 7.   Same as Figure 5, but showing the time-periodic solutions of Figure 6 instead of the Stokes waves of Figure 4. The Stokes waves generate new background radiation with each collision while the time-periodic solutions are synchronized with the background waves to avoid generating additional disturbances.

We minimize $\tilde{f}$ subject to the constraint $\eta(0,0) = 0.0707148$, the third case described in §3 for specifying the amplitude. This causes $\tilde{f}$ to decrease from 2.3×10^{-8} to 4.26×10^{-27} using $M = 1200$ grid points and $N = 1200$ time-steps (to $t = T$). The results are shown in the left panel of Figures 6 and 7. The main difference between the Stokes collision and this nearby time-periodic solution is that the Stokes waves generate additional background ripples each time they collide while the time-periodic solution contains an equilibrium background wave configuration that does not grow in amplitude after the collision. While the background waves in the counter-propagating case (studied in [49]) look like small-amplitude standing waves, these background waves travel to the right, but slower than either solitary

wave. After computing the $h = 0.05$ time-periodic solution, we computed 10 other solutions with nearby values of h and $\eta(0,0)$ to try to decrease the amplitude of the background radiation. The best solution we found (in the sense of small background radiation) is shown in the right panel of Figures 6 and 7, with $h = 0.0503$ and $\eta(0,0) = 0.0707637$. The amplitude of the background waves of this solution are comparable to that of the Stokes waves after two collisions.

Our second example is a relative periodic solution in which the initial Stokes waves (the starting guess) are B and C in Figure 1 instead of A and C. As before, solution C is shifted by π when the waves are combined initially, just as in (4.1). Because the amplitude of the larger wave has been reduced, the difference in wave speeds is smaller, and it takes much longer for the waves to collide. If the waves did not interact, we would have

$$(4.2) \qquad c_{B,0} = 0.23246089, \quad c_{C,0} = 0.22808499, \quad T_0 = \frac{2\pi}{c_{B,0} - c_{A,0}} = 1435.86,$$

where wave B crosses the domain 53.1230 times in time T_0 while wave C crosses the domain 52.1230 times. The subscript 0 indicates that the waves are assumed not to interact. Since the waves do interact, we have to evolve the solution numerically to obtain useful estimates of T and θ. We arbitrarily rounded T_0 to 1436 and made plots of the solution at times $\Delta t = T_0/1200$. We found that η is nearly even (up to a spatial phase shift) for the first time at $463\Delta t = 554.057$. This was our initial guess for $T/2$. The phase shift required to make $\eta(x + \theta/2, T/2)$ approximately even and $\varphi(x + \theta/2, T/2)$ approximately odd was found by graphically solving $\varphi(x, T/2) = 0$. This gives the initial guess $\theta/2 = 2.54258$. This choice of T and θ (with η^{B+C} and φ^{B+C} as initial conditions) yields $f = 2.0 \times 10^{-11}$ and $\tilde{f} = 1.5 \times 10^{-10}$. We then minimize f holding E and θ constant, which gives $f = 2.1 \times 10^{-29}$ and $\tilde{f} = 3.0 \times 10^{-26}$. We note that $\tilde{f}$ is computed over $[0, T]$, twice the time over which the solution was optimized by minimizing f, and provides independent confirmation of the accuracy of the solution and the symmetry arguments of §3.1.

The results are plotted in Figure 8. We omit a plot of the initial guess (the collision of Stokes waves) as it is indistinguishable from the minimized solution. In fact, the relative change in the wave profile and velocity potential is about 0.35 percent,

$$(4.3) \qquad \left(\frac{\|\eta_{\text{Stokes}} - \eta_{\text{periodic}}\|^2 + \|\varphi_{\text{Stokes}} - \varphi_{\text{periodic}}\|^2}{\|\eta_{\text{Stokes}} - h\|^2 + \|\varphi_{\text{Stokes}}\|^2} \right)^{1/2} \leq 0.0035,$$

and $T/2$ changes even less, from 554.057 (Stokes) to 554.053 (periodic). By construction, E and $\theta/2$ do not change at all. It was not necessary to evolve the Stokes waves to $T/2$, shift space by $\theta/2$, zero out Fourier modes that violate the symmetry condition (3.1), and reset $t = 0$ to correspond to this new initial state. Doing so increases the decay rate of the Fourier modes (slope of $\ln |\hat{\eta}_k|$ vs k) by a factor of 1.24 in this example, compared to 3.36 in the previous example, where it is definitely worthwhile.

The large change from $T_0/2 = 717.93$ to $T/2 = 554.053$ is due to nonlinear interaction of the waves. There are two main factors contributing to this change in period. The first is that the waves do not fully combine when they collide. Instead, the trailing wave runs into the leading wave, passing on much of its amplitude and speed. The peaks remain separated by a distance of $d = 0.52462$ at $t = T/2$, the transition point where the waves have the same amplitude. Thus, the peak separation changes by $\pi - d$ rather than π in half a period. The second effect is
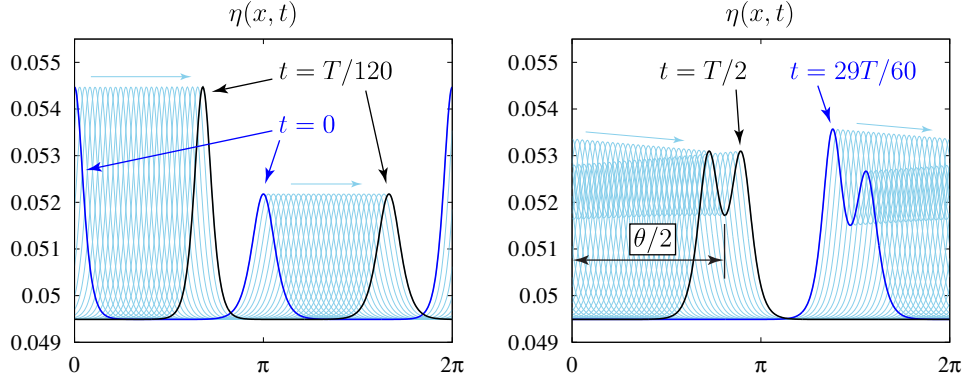
FIGURE 8.   A relative-periodic solution found using a superposi-
tion of the Stokes waves labeled B and C in Figure 1 as a starting
guess. Unlike the previous case, the waves do not fully merge at
$t = T/2$.

that the larger wave slows down the smaller wave more than the smaller slows the
larger. Recall from Fig. 2 that each wave induces a negative potential gradient
across the other wave that generates a background flow opposing its direction of
travel. Quantitatively, when the waves are well separated, we find that the taller and
smaller waves travel at speeds $c_B = 0.231077 = 0.994049c_{B,0}$ and $c_C = 0.226153 = 0.991531c_{C,0}$, respectively. The relative speed is then $(c_B - c_C) = 1.12526(c_{B,0} - c_{C,0})$. Thus,

$$(4.4) \qquad \frac{\pi - d}{c_B - c_C} < \frac{T}{2} < \frac{\pi - d}{c_{B,0} - c_{C,0}} < \frac{T_0}{2} = \frac{\pi}{c_{B,0} - c_{C,0}},$$

with numerical values $531.5 < 554.1 < 598.0 < 717.9$. This means that both effects
together have overestimated the correction needed to obtain T from T_0. This is
because the relative speed slows down as the waves approach each other, which is
expected since the amplitude of the trailing wave decreases and the amplitude of
the leading wave increases in this interaction regime. Indeed, the average speed of
the waves is

$$(4.5) \quad \overline{c_B} = \frac{\theta/2 - d/2}{T/2} = 0.993388c_{B,0}, \qquad \overline{c_C} = \frac{\theta/2 + d/2 - \pi}{T/2} = 0.991737c_{C,0},$$

which are slightly smaller and larger, respectively, than their speeds when well
separated. Note that $T/2$ in (4.4) may be written $T/2 = (\pi - d)/(\overline{c_B} - \overline{c_C})$. We
used $\theta/2 = 2.54258 + 40\pi$ in (4.5) to account for the 20 times the waves cross the
domain $(0, 2\pi)$ in time $T/2$ in addition to the offset shown in Figure 8.

5. Comparison with KdV

In the previous section, we observed two types of overtaking collisions for the
water wave: one in which the larger wave completely subsumes the smaller wave for
a time, and one where the two waves remain distinct throughout the interaction.
Similar behavior has of course been observed for the Korteweg-de Vries equation,
which was part of our motivation for looking for such solutions. Lax [32] clas-
sified overtaking collisions of two KdV solitons as bimodal, mixed, or unimodal.
Unimodal and bimodal waves are analogous to the ones we computed above, while

mixed mode collisions have the larger wave mostly subsume the smaller wave at the beginning and end of the interaction, but with a two-peaked structure re-emerging midway through the interaction. Lax showed that if $1 < c_1/c_2 < A = (3 + \sqrt{5})/2$, the collision is bimodal; if $c_1/c_2 > 3$, the collision is unimodal; and if $A < c_1/c_2 < 3$, the collision is mixed. Here c_1 and c_2 are the wave speeds of the trailing and leading waves, respectively, at $t = -\infty$. Leveque [33] has studied the asymptotic dynamics of the interaction of two solitons of nearly equal amplitude. Zou and Su [53] performed a computational study of overtaking water wave collisions, compared the results to KdV interactions, and found that the water wave collisions ceased to be elastic at third order. Craig *et. al.* [15] also found that solitary water waves collide inelastically. This does not conflict with our results since we optimize the initial conditions to make the collision elastic. Head on collisions have been studied numerically by Su and Mirie [44, 38], experimentally by Maxworthy [35], and by a mixture of analysis and computation by Craig *et. al.* [15].

Validation of KdV as a model of water waves has also been studied extensively. A formal derivation may be found in Ablowitz and Segur [1]. Rigorous justification has been given by Bona, Colin and Lannes [9], building on earlier work by Craig [14] as well as Schneider and Wayne [43]. According to [9], some gaps still exist in the theory in the spatially periodic case. Experimental studies of the validity of KdV for describing surface waves have been performed by Zabusky and Galvin [52] as well as Hammack and Segur [24]. Recently, Ostrovsky and Stepanyants [40] have compared internal solitary waves in laboratory experiments to the predictions of various model equations, including KdV, and give a comprehensive overview of the literature on this subject [40].

Our objective in this section is to determine quantitatively whether the solutions of the water wave equations that we computed in §4 are well-approximated by the KdV equation. Following Ablowitz and Segur [1], we introduce a small parameter ε and dimensionless variables

$$\hat{y} = \frac{y}{h}, \qquad \hat{x} = \sqrt{\varepsilon}\frac{x}{h}, \qquad \hat{t} = \sqrt{\frac{\varepsilon g}{h}}t, \qquad \hat{\eta} = \frac{\eta}{\varepsilon h}, \qquad \hat{\phi} = \frac{\phi}{\sqrt{\varepsilon g h^3}},$$

where h is the fluid depth. We assume the bottom boundary is at $y = -h$ rather than 0 in this derivation, so that $\hat{y}$ runs from -1 to $\varepsilon\hat{\eta}$. The Laplacian becomes $\Delta_\varepsilon = h^{-2}(\varepsilon\partial_{\hat{x}}^2 + \partial_{\hat{y}}^2)$, which allows for $\hat{\phi} = \hat{\phi}_0 + \varepsilon\hat{\phi}_1 + \varepsilon^2\hat{\phi}_2 + \cdots$ to be computed order by order, with leading terms satisfying

$$\hat{\phi}_{0,\hat{y}} = 0, \qquad \hat{\phi}_1 = -\frac{1}{2}(1 + \hat{y})^2\hat{\phi}_{0,\hat{x}\hat{x}}, \qquad \hat{\phi}_2 = \frac{1}{24}(1 + \hat{y})^4\hat{\phi}_{0,\hat{x}\hat{x}\hat{x}\hat{x}}.$$

Here we used $\Delta\phi = 0$ and $\phi_y(x, -h) = 0$. Note that $\hat{\phi}_0$ is independent of $\hat{y}$, and agrees with the velocity potential ϕ on the bottom boundary, up to rescaling:

$$\hat{\phi}_0(\hat{x}, \hat{t}) = (\varepsilon g h^3)^{-1/2}\phi(x, -h, t).$$

From the equations of motion, $\eta_t = \phi_y - \eta_x\phi_x$ and $\phi_t + \frac{1}{2}\phi_x^2 + \frac{1}{2}\phi_y^2 + g\eta = 0$, one finds that

$$\hat{\eta}_{\hat{t}} + \hat{u}_{\hat{x}} = \varepsilon\left\{\tfrac{1}{6}\hat{u}_{\hat{x}\hat{x}\hat{x}} - (\hat{\eta}\hat{u})_{\hat{x}}\right\} + O(\varepsilon^2),$$
$$\hat{u}_{\hat{t}} + \hat{\eta}_{\hat{x}} = \varepsilon\left\{\tfrac{1}{2}\hat{u}_{\hat{x}\hat{x}\hat{t}} - \tfrac{1}{2}\partial_{\hat{x}}(\hat{u})^2\right\} + O(\varepsilon^2),$$
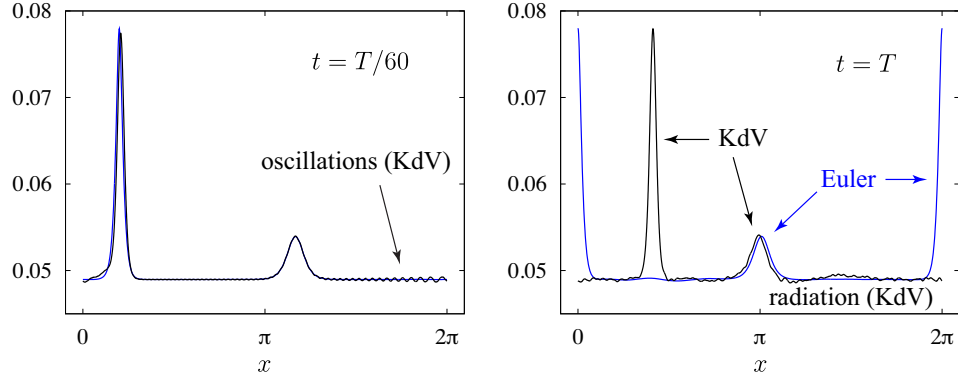
FIGURE 9. Comparison of the solutions of the KdV and Euler
equations, initialized identically with the superposition of Stokes
waves labeled A and B in Figure 1. The final time T is set to
138.399, as in Fig. 3, when the Euler solution nearly returns to its
initial configuration after a single overtaking collision.

where $\hat{u}(\hat{x},\hat{t}) = \partial_{\hat{x}}\hat{\phi}_0(\hat{x},\hat{t})$. Expanding $\hat{\eta} = \hat{\eta}_0 + \varepsilon\hat{\eta}_1 + \cdots$, $\hat{u} = \hat{u}_0 + \varepsilon\hat{u}_1 + \cdots$, we
find that

$$\hat{\eta}_0 = f(\hat{x}-\hat{t};\tau) + g(\hat{x}+\hat{t};\tau), \qquad 2f_\tau + 3ff_r + (1/3)f_{rrr} = 0,$$
$$\hat{u}_0 = f(\hat{x}-\hat{t};\tau) - g(\hat{x}+\hat{t};\tau), \qquad -2g_\tau + 3gg_l + (1/3)g_{lll} = 0,$$

where we have introduced characteristic coordinates $r = \hat{x} - \hat{t}$, $l = \hat{x} + \hat{t}$ as well as
a slow time scale $\tau = \varepsilon\hat{t}$ to eliminate secular growth in the solution with respect to
r and l at first order in ε; see [1] for details. The notational conflict of $g(l,\tau)$ with
the acceleration of gravity, g, is standard, and will not pose difficulty below.

In our case, the waves travel to the right, so we may set $g(l,\tau) = 0$ in the
formulas above. Returning to dimensional variables, we then have

$$\eta(x,t) = h\varepsilon f\left(\sqrt{\varepsilon}\left(\frac{x}{h} - \sqrt{\frac{g}{h}}t\right), \sqrt{\frac{g}{h}}\varepsilon^{3/2}t\right),$$

which satisfies

(5.1) $$\eta_t + \alpha\eta_x + \frac{3\sqrt{gh}}{2h}\eta\eta_x + \frac{1}{6}\sqrt{gh}\,h^2\eta_{xxx} = 0,$$

where $\alpha = \sqrt{gh}$. Note that ε drops out. For comparison with the results of
§4, we will add h to η and set $\alpha = -\frac{1}{2}\sqrt{gh}$ instead. In Figure 9, we compare
the solution of (5.1), with initial condition $\eta(x,0) = \eta_0^{A+B}(x)$, defined similarly to
$\eta_0^{A+C}(x)$ in (4.1), to the solution of the free-surface Euler equations shown in Figs. 3
and 4. Shortly after the waves are set in motion, the KdV solution develops high-
frequency oscillations behind the larger peak that travel left and quickly fill up the
computational domain with radiation. The solution of the Euler equations remains
much smoother. The large peak of the KdV solution also travels 3.4% faster, on
average, than the corresponding peak of the Euler solution, so that at $t = 138.399$,
when the taller Euler wave has traversed the domain 6 times, the taller KdV wave
has traversed it 6.206 times. For our purposes, these discrepancies are much too
large for KdV to be a useful model, and we conclude that the first example in §4 is
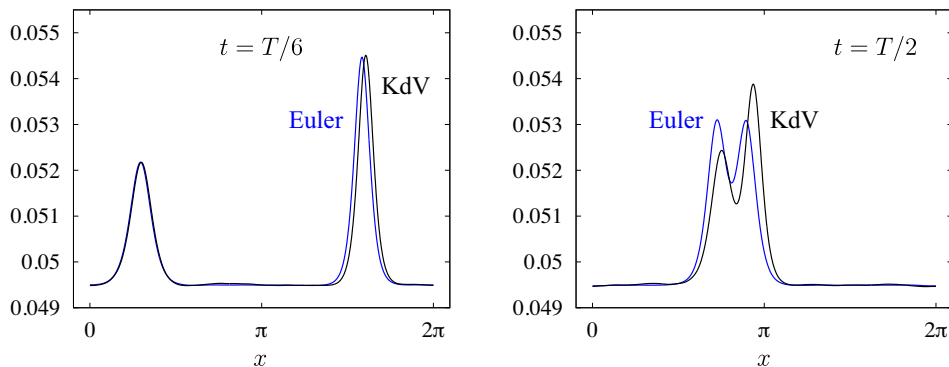well outside of the KdV regime.

FIGURE 10.   Comparison of the solutions of the KdV and Euler
equations, both initialized with the superposition of Stokes waves
labeled B and C in Figure 1. $T = 1108.11$ here.

In this comparison, timestepping the KdV equation was done with the 8 stage,
5th order implicit/explicit Runge-Kutta method of Kennedy and Carpenter [**28**].
Spatial derivatives were computed spectrally using the 36th order filter of Hou and
Li [**25**]. We found that 2048 spatial grid points and 96000 timesteps was sufficient
to reduce the error at $t = 138.399$ below 5×10^{-6} near the larger peak and below
6×10^{-7} elsewhere, based on comparing the solution to one with 3072 grid points and
192000 timesteps. Our solutions of the Euler equations are much more accurate
since there are no second or third spatial derivative terms present to make the
equations stiff. Thus, we can use 8th or 15th order explicit timestepping rather
than 5th order implicit/explicit timestepping. Monitoring energy conservation and
performing mesh refinement studies suggests that we obtain 13–14 digits of accuracy
in the solutions of the Euler equations, at which point roundoff error prevents
further improvement in double-precision arithmetic.

In Figure 10, we repeat this computation using initial conditions corresponding
to the superposition of Stokes waves $\eta_0^{B+C}(x)$, which was used as a starting guess
for the second example of §4. This time the KdV solution does not develop visible
high-frequency radiation in the wave troughs, and the solutions of KdV and Euler
remain close to each other for much longer. However, the interaction time for a
collision also increases, from $T = 138.399$ in the first example to $T = 1108.11$ here.
In Fig. 10, by $t = T/6$, the taller KdV and Euler waves have visibly separated from
each other, and by $t = T/2$, when the Euler waves have reached their minimum
approach distance, the KdV solution is well ahead of the Euler solution. Thus,
while there is good qualitative agreement between the KdV and Euler solutions,
they do not agree quantitatively over the time interval of interest. From this point
of view, the second example of §4 also lies outside of the KdV regime.

An alternative measure of the agreement between KdV and Euler is to compare
the solutions from §4 with nearby relative-periodic solutions of KdV. In other words,
we wish to quantify how much the initial conditions and period have to be perturbed
to convert a relative-periodic solution of the Euler equations into one for the KdV
equations. Since we used a superposition of Stokes waves for the initial guess to
find time-periodic and relative-periodic solutions of the Euler equations, we will
use a similar superposition (of cnoidal waves) for KdV. The vertical crest-to-trough

heights of the three Stokes waves considered in §4 are

(5.2) $H_A = 0.028918699, \qquad H_B = 0.004973240, \qquad H_C = 0.002683648.$

Well-known [**29, 20**] periodic traveling wave solutions of (5.1) are given by

$$\eta(x,t) = h - H + \frac{H}{m}\left(1 - \frac{E(m)}{K(m)}\right) + H\,\mathrm{cn}^2\left(2K(m)\frac{x-ct}{\lambda}\,\bigg|\,m\right),$$

$$\lambda = \sqrt{\frac{16mh^3}{3H}}\,K(m), \qquad c = \left[1 - \frac{H}{2h} + \frac{H}{mh}\left(1 - \frac{3E(m)}{2K(m)}\right)\right]\sqrt{gh},$$

where we added h to η to match the change in α from $\sqrt{gh}$ to $-\frac{1}{2}\sqrt{gh}$ in (5.1). Here $K(m)$ and $E(m)$ are the complete elliptic integrals of the first and second kind, respectively, and $\mathrm{cn}(z|m)$ is one of the Jacobi elliptic functions [**20, 22**]. In our case $\lambda = 2\pi$, $g = 1$ and $h = 0.05$. For each H in (5.2), we solve the λ equation for m using Mathematica [**51**], and then evaluate $\eta(x,0)$ on a uniform grid that is fine enough that its Fourier coefficients decay below machine roundoff. The values of $m' = 1 - m$ are

$$m'_A = 1.81924 \times 10^{-35}, \qquad m'_B = 1.98689 \times 10^{-14}, \qquad m'_C = 1.79643 \times 10^{-10}.$$

This approach requires extended precision arithmetic to compute m and evaluate η, but the running time takes only a few seconds on a typical laptop. A periodized version of the simpler sech^2 formula could be used for the first two waves, but decays too slowly for wave C to be spatially periodic to roundoff accuracy. Once these cnoidal waves have been computed, we superpose their initial conditions to form η_0^{A+B} and η_0^{B+C}, just as in §4. It is well-known that a superposition of N cnoidal waves retain this form when evolved via KdV, with N amplitude and N phase parameters governed by an ODE describing pole dynamics in the complex plane [**31, 2, 19**]. In the $N = 2$ case, the solutions are relative-periodic.

Figures 11 and 12 compare the time-periodic and relative-periodic solutions of the Euler equations, computed in §4, to these cnoidal solutions of KdV. Since the periods are different, only the initial conditions are compared. In the larger-amplitude example, shown in Fig. 11, the Euler solution is not as flat in the wave trough as the cnoidal solution due to an additional oscillatory component (the "tuned" radiation). From the difference plot in the right panel, we see that the crest-to-trough amplitude of these higher frequency oscillations is roughly 6×10^{-4}, or 2.1% of the wave height H_A. The Euler solution is time-periodic with period $T_{\mathrm{Euler}} = 138.387$ while the cnoidal solution is relative-periodic, returning to a spatial phase shift of its initial condition at $T_{\mathrm{KdV}} = 113.079$, which differs from T_{Euler} by 18%. In the smaller-amplitude example, shown in Fig. 12, both solutions have smooth, flat wave troughs, and it is difficult to distinguish one from the other in the left panel. The crest-to-trough amplitude of the difference in the right panel is roughly 5.5×10^{-5}, or 1.1% of H_B. The relative change in period is $(T_{\mathrm{Euler}} - T_{\mathrm{KdV}})/T_{\mathrm{Euler}} = 3.6\%$. While the left panels of Figures 11 and 12 show close agreement between relative-periodic solutions of the Euler and KdV equations at $t = 0$, it should be noted that the wave amplitudes of the cnoidal solutions were chosen to minimize the discrepancy in these figures. The change in period by 18% and 3.6%, respectively, is perhaps a better measure of agreement.

A final comparison of the two equations is made in Fig. 13, where we evolve the Euler equations with the KdV initial conditions. This requires an initial condition for $\varphi(x) = \phi(x, \eta(x))$, where we have suppressed t in the notation for this
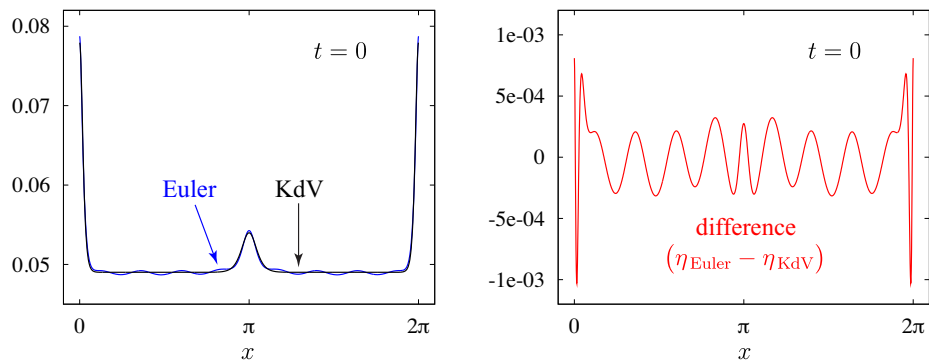
FIGURE 11. Comparison of time-periodic solution found in §4 to nearby relative-periodic two phase cnoidal solution of KdV. The periods are $T = 138.387$ and 113.079, respectively.
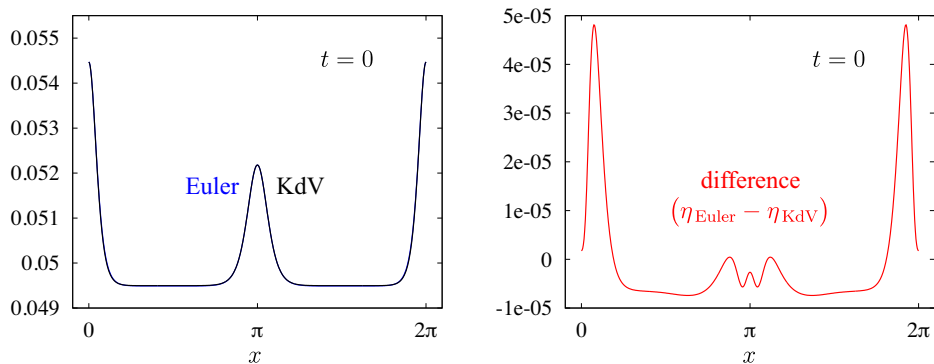

FIGURE 12. Comparison of relative-periodic solution found in §4 to nearby relative-periodic two phase cnoidal solution of KdV. The periods are $T = 1108.11$ and 1068.73, respectively.
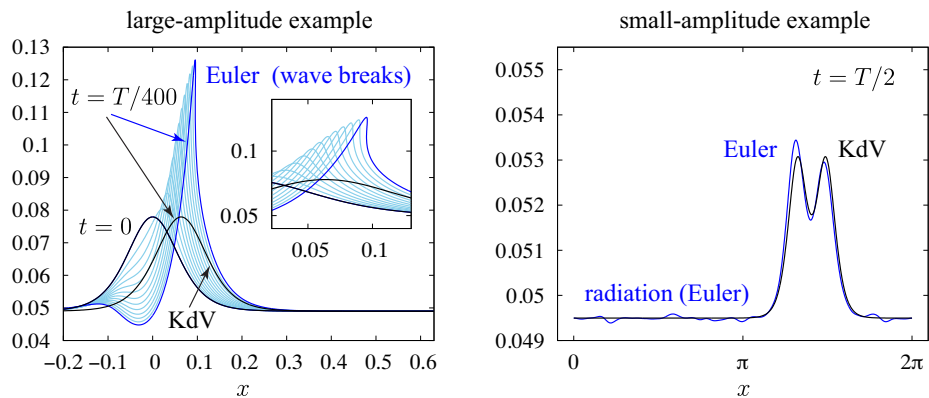

FIGURE 13. Comparison of KdV and Euler solutions, both initialized with a 2-phase cnoidal wave with peaks matching the heights of the Stokes waves labeled A and B (left) or B and C (right) in Fig. 1. Here $T = 138.387$ (left) and $T = 1068.73$ (right).

discussion since it is held fixed at 0. Based on the derivation presented above, we first solve $\phi_x(x,0) = \sqrt{g/h}[\eta(x) - h]$ for ϕ on the bottom boundary. We then use the approximation

$$\varphi(x) \approx \phi(x,0) - \frac{\eta(x)^2}{2}\phi_{xx}(x,0) + \frac{\eta(x)^4}{24}\phi_{xxx}(x,0)$$

to evaluate ϕ on the free surface. In the left panel of Figure 13, the larger wave grows and overturns before $t = T/400$ when evolved under the Euler equations, instead of traveling to the right when evolved via KdV. To handle wave breaking, we switched to an angle-arclength formulation of the free-surface Euler equations [**26, 4**]. In the small-amplitude example in the right panel, the Euler solution develops visible radiation and falls slightly behind the KdV solution, although the phases are closer at $T/2$ than the result of evolving the Stokes waves under KdV in Figure 10. We also tried evaluating

$$\phi(x,y) = \sqrt{g/h}\sum_{k=1}^{\infty} 2k^{-1}\hat{\eta}_k \sin(kx)\cosh(ky)$$

at $y = \eta(x)$ to obtain the initial condition for $\varphi(x)$, where $\hat{\eta}_k$ are the Fourier modes of $\eta(x)$ at $t = 0$, but the results were worse for the large-amplitude example — the wave breaks more rapidly — and were visually indistinguishable in the small-amplitude example from the results plotted in Fig. 13.

In summary, the large-amplitude time-periodic solution of the Euler equations found in §4 is well outside of the KdV regime by any measure, and the small-amplitude relative-periodic solution is closer, but not close enough to achieve quantitative agreement over the entire time interval of interest.

6. Conclusion

We have demonstrated that the small amount of background radiation produced when two Stokes waves interact in shallow water can often be tuned to obtain time-periodic and relative-periodic solutions of the free-surface Euler equations. Just as for the Korteweg-de Vries equation, the waves can fully merge when they collide or remain well-separated. However, the comparison is only qualitative as the waves are too large to be well-approximated by KdV theory.

In future work, we will study the stability of these solutions using Floquet theory. Preliminary results suggest that the first example considered above is unstable to harmonic perturbations while the second example is stable. In the stable case, an interesting open question is whether the Stokes waves used as a starting guess for the minimization algorithm, which have the same energy as the relative-periodic solution found, might remain close to it forever, executing almost-periodic oscillations around it. Presumably θ would need to be varied slightly for this to be true, since θ is a free parameter that we selected by hand to obtain a small value of $\tilde{f}$ for the initial guess. Another open question is whether there are analogues for the Euler equations of N-phase quasi-periodic solutions of the KdV equation with $N \geq 3$. We are confident that the methods of this paper could be used to construct degenerate cases of $N \geq 3$ solitary water waves colliding elastically in a time-periodic or relative-periodic fashion, along the lines of what was done for the Benjamin-Ono equation in [**3**]. Computing more general quasi-periodic dynamics of the form $\eta(x,t) = H(\vec{\kappa}x + \vec{\omega}t + \vec{\alpha})$, $\varphi(x,t) = \Phi(\vec{\kappa}x + \vec{\omega}t + \vec{\alpha})$ with $H, \Phi \in C(\mathbb{T}^N)$ and $\vec{\kappa}, \vec{\omega}, \vec{\alpha} \in \mathbb{R}^N$ seems possible in principle using a more sophisticated shooting

method to determine H, Φ and $\vec{\omega}$. Existence of such solutions for the Euler equations would show that non-integrable equations can also support recurrent elastic collisions even if they cannot be represented as N-phase superpositions of elliptic functions.

References

1. Mark J. Ablowitz and Harvey Segur, *Solitons and the inverse scattering transform*, SIAM, Philadelphia, 1981.
2. H. Airault, H. P. McKean, and J. Moser, *Rational and elliptic solutions of the Korteweg-de Vries equation and a related many-body problem*, Comm. Pure Appl. Math. **30** (1977), 95–148.
3. D. M. Ambrose and J. Wilkening, *Global paths of time-periodic solutions of the Benjamin–Ono equation connecting pairs of traveling waves*, Comm. App. Math. and Comp. Sci. **4** (2009), no. 1, 177–215.
4. ———, *Computation of symmetric, time-periodic solutions of the vortex sheet with surface tension*, Proc. Nat. Acad. Sci. **107** (2010), no. 8, 3361–3366.
5. ———, *Computation of time-periodic solutions of the Benjamin–Ono equation*, J. Nonlinear Sci. **20** (2010), no. 3, 277–308.
6. ———, *Dependence of time-periodic votex sheets with surface tension on mean vortex sheet strength*, Procedia IUTAM **11** (2014), 15–22.
7. G. R. Baker, D. I. Meiron, and S. A. Orszag, *Generalized vortex methods for free-surface flow problems*, J. Fluid Mech. **123** (1982), 477–501.
8. G. R. Baker and C. Xie, *Singularities in the complex physical plane for deep water waves*, J. Fluid Mech. **685** (2011), 83–116.
9. J. L. Bona, T. Colin, and D. Lannes, *Long wave approximations for water waves*, Arch. Rational Mech. Anal. **178** (2005), 373–410.
10. R. K.-C. Chan and R. Street, *A computer study of finite amplitude water waves*, J. Comput. Phys. **6** (1970), 68–94.
11. G. A. Chandler and I. G. Graham, *The computation of water waves modelled by Nekrasov's equation*, SIAM J. Numer. Anal. **30** (1993), no. 4, 1041–1065.
12. B. Chen and P. G. Saffman, *Numerical evidence for the existence of new types of gravity waves of permanent form on deep water*, Stud. Appl. Math. **62** (1980), 1–21.
13. M. J. Cooker, P. D. Weidman, and D. S. Bale, *Reflection of a high-amplitude solitary wave at a vertical wall*, J. Fluid Mech. **342** (1997), 141–158.
14. W. Craig, *An existence theory for water waves and the Boussinesq and Korteweg-de Vries scaling limits*, Comm. Partial Diff. Equations **10** (1985), 787–1003.
15. W. Craig, P. Guyenne, J. Hammack, D. Henderson, and C. Sulem, *Solitary water wave interactions*, Phys. Fluids **18** (2006), 057106.
16. W. Craig and C. Sulem, *Numerical simulation of gravity waves*, J. Comput. Phys. **108** (1993), 73–83.
17. A. D. D. Craik, *The origins of water wave theory*, Ann. Rev. Fluid Mech. **36** (2004), 1–28.
18. ———, *George gabriel stokes on water wave theory*, Ann. Rev. Fluid Mech. **37** (2005), 23–42.
19. B. Deconinck and H. Segur, *Pole dynamics for elliptic solutions of the KdV equation*, Mathematical Physics, Analysis and Geometry **3** (2000), 49–74.
20. Maarten W. Dingemans, *Water wave propagation over uneven bottoms, part 2. non-linear wave propagation*, World Scientific, Singapore, 1997.
21. S. Govindjee, T. Potter, and J. Wilkening, *Cyclic steady states of treaded rolling bodies*, Int. J. Numer. Meth. Engng. (2014), (accepted).
22. I. S. Gradshteyn and I. M. Ryzhik, *Table of integrals, series and products*, 7th ed., Academic Press, Amsterdam, 2007.
23. E. Hairer, S. P. Norsett, and G. Wanner, *Solving ordinary differential equations I: Nonstiff problems, 2nd edition*, Springer, Berlin, 2000.
24. J. L. Hammack and H. Segur, *The Korteweg-de Vries equation and water waves. part 2. comparison with experiments*, J. Fluid Mech. **65** (1974), 289–314.
25. T. Y. Hou and R. Li, *Computing nearly singular solutions using pseudo-spectral methods*, J. Comput. Phys. **226** (2007), 379–397.
26. T. Y. Hou, J. S. Lowengrub, and M. J. Shelley, *Removing the stiffness from interfacial flows with surface tension*, J. Comput. Phys. **114** (1994), 312–338.

27. R. S. Johnson, *A modern introduction to the mathematical theory of water waves*, Cambridge University Press, Cambridge, UK, 1997.

28. C. A. Kennedy and M. H. Carpenter, *Additive Runge-Kutta schemes for convection-diffusion-reaction equations*, Appl. Numer. Math. **44** (2003), no. 1–2, 139–181.

29. D. J. Korteweg and G. de Vries, *On the change of form of long waves advancing in a rectangular canal, and on a new type of long stationary waves*, Philosophical Magazine **39** (1895), 422–443.

30. R. Krasny, *Desingularization of periodic vortex sheet roll-up*, J. Comput. Phys. **65** (1986), 292–313.

31. M. D. Kruskal, *The Korteweg-de Vries equation and related evolution equations*, Nonlinear wave motion, Lectures in Appl. Math., vol. 15, American Mathematical Society, Providence, 1974, pp. 61–83.

32. P. D. Lax, *Integrals of nonlinear equations of evolution and solitary waves*, Comm. Pure Appl. Math. **21** (1968), 467–490.

33. R. J. LeVeque, *On the interaction of nearly equal solitons in the kdv equation*, SIAM J. Appl. Math. **47** (1987), 254–262.

34. M. S. Longuet-Higgins and E. D. Cokelet, *The deformation of steep surface waves on water. I. a numerical method of computation*, Proc. Royal Soc. A **350** (1976), 1–26.

35. T. Maxworthy, *Experiments on collisions between solitary waves*, J. Fluid Mech. **76** (1976), 177–185.

36. G N Mercer and A J Roberts, *Standing waves in deep water: Their stability and extreme form*, Phys. Fluids A **4** (1992), no. 2, 259–269.

37. P. A. Milewski, J.-M. Vanden-Broeck, and Z. Wang, *Dynamics of steep two-dimensional gravity–capillary solitary waves*, J. Fluid Mech. **664** (2010), 466–477.

38. R. M. Mirie and C. H. Su, *Collisions between two solitary waves, Part II*, J. Fluid Mech. **115** (1982), 475–492.

39. J. Nocedal and S. J. Wright, *Numerical optimization*, Springer, New York, 1999.

40. L. A. Ostrovsky and Y. A. Stepanyants, *Internal solitons in laboratory experiments: Comparison with theoretical models*, Chaos **15** (2005), 037111:1–28.

41. P. Plotnikov and J. Toland, *Nash-moser theory for standing water waves*, Arch. Rat. Mech. Anal. **159** (2001), 1–83.

42. Chris H. Rycroft and Jon Wilkening, *Computation of three-dimensional standing water waves*, J. Comput. Phys. **255** (2013), 612–638.

43. G. Schneider and C. E. Wayne, *The long-wave limit for the water wave problem. i. the case of zero surface tension*, Comm. Pure Appl. Math. **53** (2000), 1475–1535.

44. C. H. Su and R. M. Mirie, *On head-on collisions between two solitary waves*, J. Fluid Mech. **98** (1980), 509–525.

45. J.-M. Vanden-Broeck, *Elevation solitary waves with surface tension*, Phys. Fluids A **3** (1991), 1989–1993.

46. G. B. Whitham, *Linear and nonlinear waves*, Wiley, New York, 1974.

47. J. Wilkening, *Breakdown of self-similarity at the crests of large amplitude standing water waves*, Phys. Rev. Lett **107** (2011), 184501.

48. _____, *Traveling-standing water waves*, (2014), (in preparation).

49. J. Wilkening and J. Yu, *Overdetermined shooting methods for computing standing water waves with spectral accuracy*, Comput. Sci. Disc. **5** (2012), 014017:1–38.

50. M. O. Williams, J. Wilkening, E. Shlizerman, and J. N. Kutz, *Continuation of periodic solutions in the waveguide array mode-locked laser*, Physica D **240** (2011), no. 22, 1791–1804.

51. Wolfram Research, Inc, *Mathematica, version 8.0*, Champaign, IL, 2010.

52. N. J. Zabusky and C. J. Galvin, *Shallow-water waves, the Korteweg-de Vries equation and solitons*, J. Fluid Mech. **47** (1970), 811–824.

53. Q. Zou and C. H. Su, *Overtaking collisions between two solitary waves*, Phys. Fluids **29** (1986), 2113–2123.

DEPT OF MATHEMATICS, UNIVERSITY OF CALIFORNIA, BERKELEY, CA 94720-3840
E-mail address: `wilkening@berkeley.edu`